Check for updates

A Co-MOF-derived Co$_9$S$_8$@NS-C electrocatalyst for efficient hydrogen evolution reaction†

Yun-Wu Li, [ID]* Qian Wu, Rui-Cong Ma, Xiao-Qi Sun, Dan-Dan Li, Hong-Mei Du, Hui-Yan Ma,* Da-Cheng Li, Su-Na Wang [ID]* and Jian-Min Dou

The exploitation of efficient hydrogen evolution reaction (HER) electrocatalysts has become increasingly urgent and imperative; however, it is also challenging for high-performance sustainable clean energy applications. Herein, novel Co$_9$S$_8$ nanoparticles embedded in a porous N,S-dual doped carbon composite (abbr. Co$_9$S$_8$@NS-C-900) were fabricated by the pyrolysis of a single crystal **Co-MOF** assisted with thiourea. Due to the synergistic benefit of combining Co$_9$S$_8$ nanoparticles with N,S-dual doped carbon, the composite showed efficient HER electrocatalytic activities and long-term durability in an alkaline solution. It shows a small overpotential of −86.4 mV at a current density of 10.0 mA cm^{-2}, a small Tafel slope of 81.1 mV dec^{-1}, and a large exchange current density (J_0) of 0.40 mA cm^{-2}, which are comparable to those of Pt/C. More importantly, due to the protection of Co$_9$S$_8$ nanoparticles by the N,S-dual doped carbon shell, the Co$_9$S$_8$@NS-C-900 catalyst displays excellent long-term durability. There is almost no decay in HER activities after 1000 potential cycles or it retains 99.5% of the initial current after 48 h.

1. Introduction

Due to the energy crisis and environmental problems, sustainable utilization of renewable energy has shown rapid development in the world. As high efficiency and clean energy, hydrogen energy is giving rise to a new dawn in the future energy systems and is well on the way.[1,2] Thus, exploring numerous HER electrocatalysts to generate sufficient H$_2$ by water-splitting is an effective and efficient tactic.[1,2] It is know that noble metal Pt is by far the most efficient and benchmark HER electrocatalyst; however, it suffers from resource exhaustion, which blocks its widespread applications.[3,4] Therefore, various alternative noble-metal-free catalysts, such as transition metal derived nanomaterials (Mo, W, Co, Fe, and Ni),[5–10] N, S, P heteroatom-doped carbon materials,[11] and their composites,[12] have been scrutinized due to their high HER electrocatalytic activities, other important energy storage and conversion features,[13] and low cost. Of note, Co(II)-based species are a type of high-profile candidates whose enhanced electrocatalytic activities have recently been noticed.[7,8,14,15] Among them, cobalt and sulfide-rich Co$_9$S$_8$ have been applied in both electrocatalytic ORR and various batteries but scarcely in HER due to its low

conductivity and easy aggregation.[14,15] To improve these defects, encapsulating metal sulfides into N or S doped carbon materials to generate hybrids gave us a profound inspiration.[11] The heteroatom-doped carbon materials not only offer improved electrical conductivity, long-term durability and high selectivity but also can be used as shells to protect metal sulfides from aggregation. More specifically, N,S-dual doped carbon materials themselves have been employed as attractive HER electrocatalysts.[11] Therefore, combining Co$_9$S$_8$ nanoparticles and N,S-dual doped carbon to prepare new composite materials and further improve their HER electrocatalytic activities is indeed an appealing task.[15]

In recent years, metal–organic framework (MOF)-derived hybrids are demonstrated as promoting electrocatalysts for energy storage and conversion.[16,17] By pyrolysis of MOF precursors, the advanced features of MOFs, such as heteroatom-doped carbon skeletons, active metal nodes, adjustable structure components, robust frameworks, and periodic porosities, can be endowed or transferred into the derived hybrids with advantages toward electrocatalysis.[16,17] To promise highly active electrocatalysts, one can also encapsulate small organic molecules containing heteroatoms to introduce and increase multiple active sites. Herein, we incorporated a small thiourea molecule with both N and S into a crystalline **Co-MOF (LCU-105)**[18] to manage multi-component composites for HER. The skeleton ligands of **Co-MOF** and thiourea offer N,S-dual doped carbon substrates, which can not only favour electrical conductivity and improve potential active sites but can also embed Co(II) species to increase stability. As a result, Co$_9$S$_8$

Shandong Provincial Key Laboratory of Chemical Energy Storage and Novel Cell Technology, School of Chemistry and Chemical Engineering, Liaocheng University, Liaocheng 252000, P. R. China. E-mail: liyunwu@lcu.edu.cn; mahuiyanyan@163.com; wangsuna@lcu.edu.cn

nanoparticles wrapped in the N,S-dual doped carbon composite (abbreviated as Co_9S_8@NS-C-900) were fabricated. The Co_9S_8@NS-C-900 composite displays efficient HER electrocatalytic activities and long-term durability. It showed a small overpotential of −86.4 mV at a 10.0 mA cm^{-2} current density, a small Tafel slope of 81.1 mV dec^{-1}, and a large exchange current density (J_0) of 0.40 mA cm^{-2}, performance comparable to Pt/C.

2. Experimental section

2.1. Chemicals and material characterization

All chemicals were purchased commercially and used as received. The powder X-ray diffraction (PXRD) was obtained on a D/MAX-rA (Rigaku) diffractometer with Cu Kα radiation ($\lambda = 1.542$ Å) at a scan rate of 4° min^{-1}. Raman spectrum was collected using Monovista CRS500. X-ray photoelectron spectra (XPS) were collected using ESCALAB Xi+. N_2 adsorption experiments were performed on a Micrometrics ASAP 2020M instrument. FT-IR spectra were recorded on a NICOLET 6700F-IR spectrometer using the KBr disc method in the range of 400–4000 cm^{-1}. Electron microscopy measurements were performed on a field-emission scanning electron microscope (SEM, JSM-6360). Transmission electron microscopy (TEM) was performed on a JEM-2100 at 200 kV.

2.2. Syntheses and structure of the Co-MOF precursor

The pure single crystals of the **Co-MOF (LCU-105)** precursor were synthesized according to our recently reported reference and for the detailed synthesis process see ESI.†[18] The pure phase was confirmed by single-crystal X-ray diffraction (Table S1, ESI†) and PXRD (Fig. S2, ESI†) measurements. The **Co-MOF** structure displays a three-dimensional (3D) microporous framework (see Scheme 1 and Fig. S1†), which can well enclose small organic molecules, such as thiourea, presenting it as an excellent candidate as a precursor to fabricate multi-component composites. The crystallographic data of **Co-MOF** are listed in Table S1 (ESI†). The synthesis details of Co_9S_8@NS-C composites can be found in Scheme 1 and are discussed below.

2.3. Fabrication of Co_9S_8@NS-C composites

The Co_9S_8@NS-C composites were synthesized using the above **Co-MOF** as a precursor *via* the pyrolysis route in Ar atmosphere, followed by the acid etching treatment (Scheme 1): (i) a mixture of crystalline **Co-MOF** and thiourea was carefully ground in an agate mortar to obtain the thiourea@**Co-MOF** precursor. (ii) The precursor was transferred to a tube furnace and carbonized under an Ar atmosphere at different temperatures (1000, 900 and 800 °C) for 3 h. The N,S-dual doped carbon composite wrapping both the CoO_x and Co_9S_8 nanoparticles was formed. (iii) The obtained three samples were thoroughly etched with 3 M HCl solutions 3 times to remove the residual CoO_x (Scheme 1), and then repeatedly rinsed in ultra-pure water and ethanol. After drying at 60 °C in a vacuum for 8 h, black catalyst powder was synthesized (Scheme 1). These samples are abbreviated as **Co-MOF**-1000, **Co-MOF**-900 and **Co-MOF**-800. The calcined **Co-**

MOF-900 (or named as Co_9S_8@NS-C-900) sample displays good HER performance and was selected to study its other characteristics.

2.4. Electrochemical measurements

The HER electrocatalytic properties including EIS (electrochemical impedance spectroscopy) were evaluated using the Gamry references 3000 electrochemical workstation. A typical experimental procedure was performed as follows: 2.0 mg of the Co_9S_8@NS-C-900 composite catalyst (or 20% Pt/C) was dispersed in 1 mL ultra-pure H_2O under ultrasound to obtain a homogeneous catalyst ink. Then, 20 μL of the catalyst ink was dropped on the glassy carbon electrode (0.196 cm^2). Afterwards, 5 μL of Nafion aqueous solution (0.5 wt%) was dropped on the electrode and naturally air-dried. A three-electrode cell system was worked out using glassy carbon as the working electrode, Ag/AgCl (4 M) as the reference electrode, graphite rod as the counter electrode, and 70 mL KOH (1 M) as the electrolyte. Linear sweep voltammogram (LSV) tests were performed at a scan rate of 10 and 5 mV s^{-1}, respectively. The long-term durability test was performed using chronopotentiometric measurements. All the potentials were calibrated to a reversible hydrogen electrode (RHE) using the equation $E_{RHE} = E_{Ag/AgCl} + 0.205$ V $+ 0.0591$ pH and without an IR-correction.
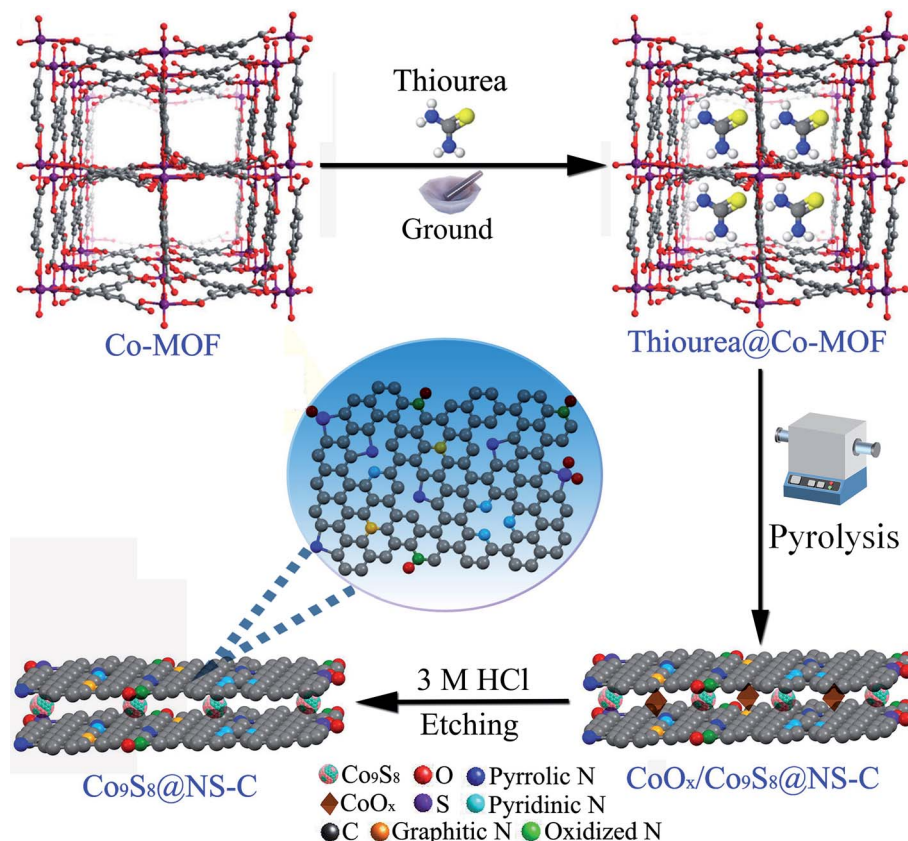
3. Results and discussions

3.1. Structural characterizations of the Co_9S_8@NS-C-900 composite

The phase composition of the as-prepared Co_9S_8@NS-C-900 was detected *via* PXRD. As shown in Fig. 1a, the characteristic peaks are well assigned to the cubic Co_9S_8 phase (PDF#73-1442). The peaks at *ca.* $2\theta = 15.43°$, $17.84°$, $29.80°$, $31.81°$, $39.52°$, $40.61°$, $44.66°$, $52.06°$, $54.62°$ and $55.5°$ are ascribed to the (111), (200), (311), (222), (331), (420), (422), (440), (531) and (600) diffraction planes of cubic Co_9S_8, respectively. Therefore, the Co_9S_8 nanoparticles embedded in NS-C was confirmed by the PXRD results. Raman spectra (Fig. 1b) of the Co_9S_8@NS-C-900 catalyst also displayed the characteristic C–C absorption signals at 1449 and 1624 cm^{-1}, indexing to D (defects or amorphous of graphitic carbon) and G (ordered sp^2 bonded graphitic carbon) bands of carbon materials, respectively. Therefore, the small I_D/I_G confirms that NS-C is partially graphitized and generates multiple defects as active sites by N,S-dual doping modification.[19a] These features of carbon-based catalysts may not only effectively improve the electronic conductivity and anti-corrosion, but also enhance the electrocatalytic efficiency.[11,12] Moreover, a broad peak with a maximum value at 2573 cm^{-1} further proved the evidence of the 2D N,S-dual doped carbon materials. The peaks at 863, 1165 and 1300 cm^{-1} can be attributed to the Co_9S_8 species.[19b,c,d] Raman spectroscopy results also further demonstrate the formation of the Co_9S_8@NS-C-900 composite. The chemical model of Co_9S_8 by the combination of PXRD and Raman is demonstrated in Fig. 1b.

As the porous framework of **Co-MOF** can be easily transmitted to its derived material, the porous feature of the

Scheme 1 The fabrication of Co$_9$S$_8$@NS-C composites by pyrolysis and etching.

Co$_9$S$_8$@NS-C-900 composite was evaluated by N$_2$ adsorption studies (Fig. 2a). The N$_2$ adsorption capacity rises rapidly at the beginning, afterward it grows slowly to reach a maximum of 90.7 cm^3 g^{-1}. The isotherm displays a clear reversible adsorption behaviour, which shows a typical type-I porous feature.[20] The corresponding BET (Brunner–Emmet–Teller) was calculated as *ca.* 239 m^2 g^{-1} using the above N$_2$ adsorption data.[20] This high BET surface area supplies the exposure of additional active sites, which are beneficial for the HER activity. The diameters of pores are between 4.4 and 19 Å, and the pore maximum is at 7.9 Å, indicating the easy transportation of H$_2$ in the electrocatalytic process appropriately.

The chemical composition of the Co$_9$S$_8$@NS-C-900 composite was further checked *via* XPS (Fig. 2b–f). The survey spectrum displays that the composite consists of Co, S, N, C and O elements (Fig. 2b). The Co 2p high-resolution spectrum after fitting displays that it comprises four typical characteristic peaks (Fig. 2c): the peaks at 777.04 and 796.75 eV are assigned to Co^{3+}; the peaks at 781.40 and 798.03 eV are ascribed to Co^{2+}. However, the peaks at 785.94 eV and 802.97 are indexed to satellite peaks.[21,22] The S 2p high-resolution spectrum is
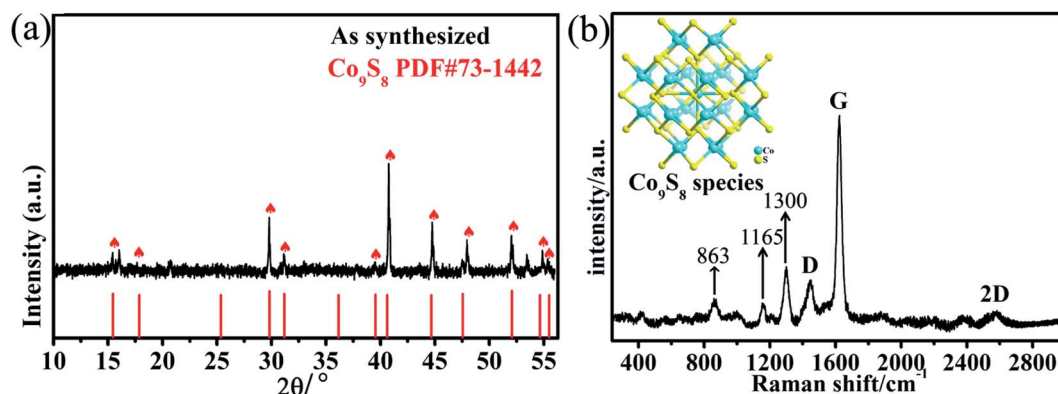

Fig. 1 The PXRD pattern (a) and (b) Raman spectrum of the Co$_9$S$_8$@NS-C-900 composite (inset: the chemical model of Co$_9$S$_8$).
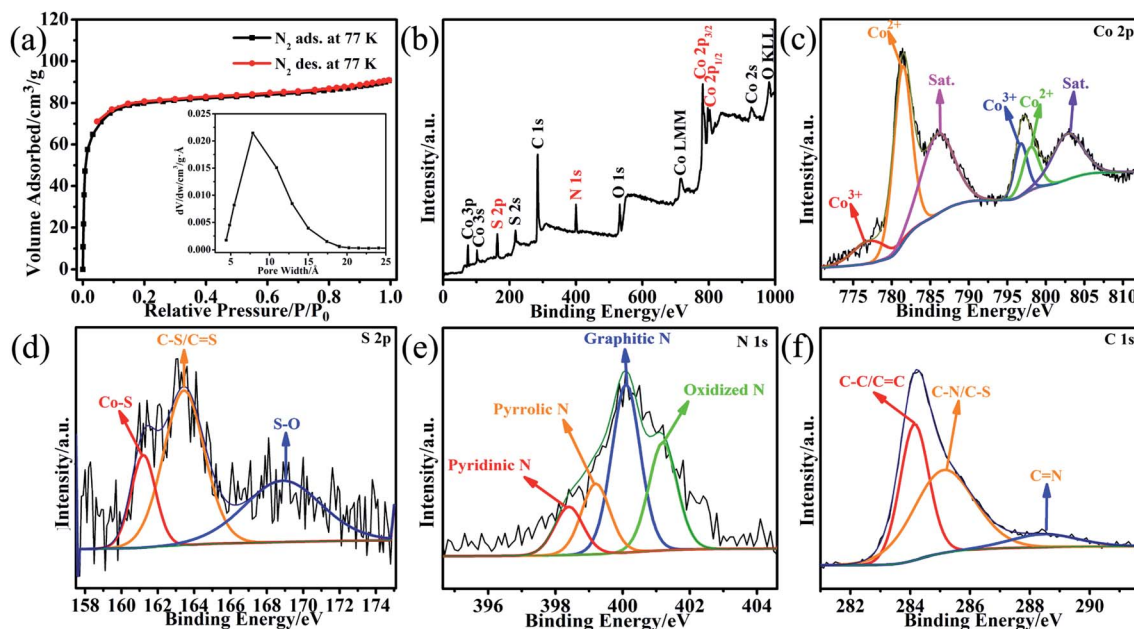
Fig. 2 (a) The N_2 sorption isotherm (inset: the pore size distribution). (b) The XPS survey spectrum. High-resolution XPS: (c) Co 2p. (d) S 2p. (e) N 1s. (f) C 1s of the Co_9S_8@NS-C-900 composite.

deconvoluted into three peaks at 161.20, 163.44 and 168.86 eV (Fig. 2d), assigning to Co–S, C–S/C=S, and C–S–O, respectively.[21,22] These peaks also verify the existence of the Co_9S_8 and N,S-dual doped carbon substance. The N 1s high-resolution spectrum contains four peaks (Fig. 2e). The peak at 398.4 eV is assigned to the pyridinic-N species, showing the formation of CoN_x active sites. The peak located at 399.2 eV corresponds to the pyrrolic-N species with another mode of CoN_x active sites. The peak at 400.1 eV is indexed to the graphitic-N species. The peak located at 401.2 eV is regarded as the oxidized-N species.[21,22] According to the literature, both pyridinic-N and pyrrolic-N can effectively regulate HER active sites.[21,22] The C 1s high-resolution spectrum is also divided into three peaks located at 284.14, 285.16 and 288.46 eV (Fig. 2f), illustrating the coexistence of C=C/C–C, C–S/C–N, and C=N, respectively.[21,22] These XPS analyses are in agreement with the above PXRD and Raman results.[19a] Such CoN_x and N,S-dual-doped carbon often offer plentiful electrochemically active sites for HER and are further responsive to better HER performance and long-term durability.[7,8,15,21,22]

FT-IR was performed to identify the chemical bonds and groups present in the Co_9S_8@NS-C-900 composite, and it confirmed the above compositional analysis results. As shown in Fig. S4 (ESI†), the weak peak at *ca.* 456 cm^{-1} and the moderate peak at 580 cm^{-1} are ascribed to Co–S and Co–N bonds, indicating the existence of Co_9S_8 and CoN_x active sites in the catalyst, respectively. A broad peak at 1039 cm^{-1} is probably the overlap bending vibrations of C–N, N–H and C–S bonds. The peak at 1402 cm^{-1} is ascribed to C–N and C–H groups. The spike peak at 1630 cm^{-1} and the broad strong peak at 3422 cm^{-1} are both identified as the bending vibrations of N–H bonds. The small peaks at 2848 and 2915 cm^{-1} are ascribed to

the C–H bonds stretching vibrations.[19d,23] These results all confirm the formation of the Co_9S_8@NS-C-900 composite by encapsulating Co_9S_8 nanoparticles in the porous N,S-dual doped carbon substrate.

3.2. Morphological analysis of the Co_9S_8@NS-C-900 composite

The morphology and microstructure of the Co_9S_8@NS-C-900 composite were evaluated using SEM and TEM, respectively. The SEM morphology of the Co_9S_8@NS-C-900 composite displays interconnected aggregates composed of nanoflakes, and their sizes were within about 10–40 μm (Fig. 3a–c). These carbon nanoflakes intertwine each other to generate porous aggregates, providing transport channels for HER. From Fig. 3c, it can be seen that Co_9S_8 nanoparticles are clearly embedded into the N,S-dual-doped nanoflakes. Furthermore, the EDS mapping proves the coexistence of Co, S, N and C elements in these carbon nanoflakes (Fig. 3d), and they are uniformly doped in the entire carbon structure. From the EDS mapping of Co and S elements, Co_9S_8 nanoparticles can be brightly shown by highlights. TEM was also performed to further characterize the detailed structural features of the as-obtained Co_9S_8@NS-C-900 composite (Fig. 4a–i). It can be observed that highly crystalline block-like Co_9S_8 nanoparticles are wrapped by the amorphous N,S-dual-doped carbon nanoflakes (Fig. 4b). High-resolution TEM images also indicate that the composite co-exists in two types of planes: one is the Co_9S_8 crystalline phase and the other is the N,S-dual doped carbon amorphous phase (Fig. 4c,d). From Fig. 4c and d, a characteristic lattice plane distance *ca.* 0.497 nm was observed, which can be ascribed to the (200) plane of the cubic Co_9S_8 phase.[14,15] This analysis coincides with PXRD results. Moreover, from the
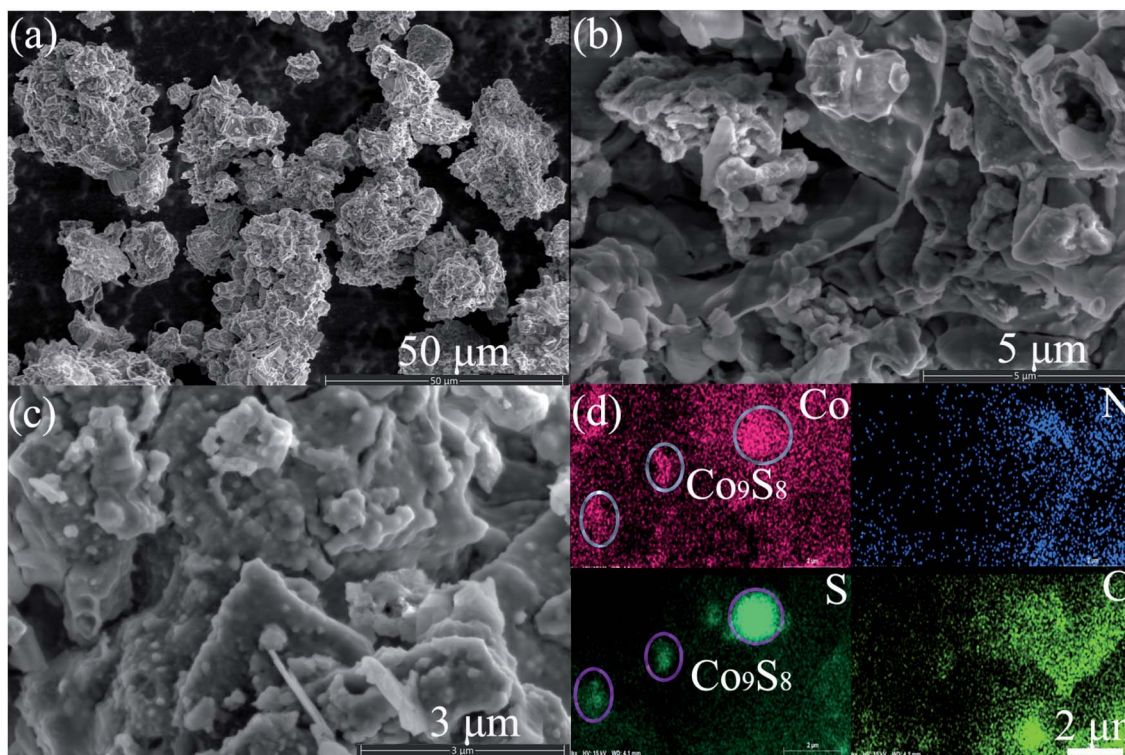
Fig. 3 (a–c) The SEM images of the Co_9S_8@NS-C-900 composite under different magnifications. (d) The EDS mapping images of selected regions: Co, S, N, and C.
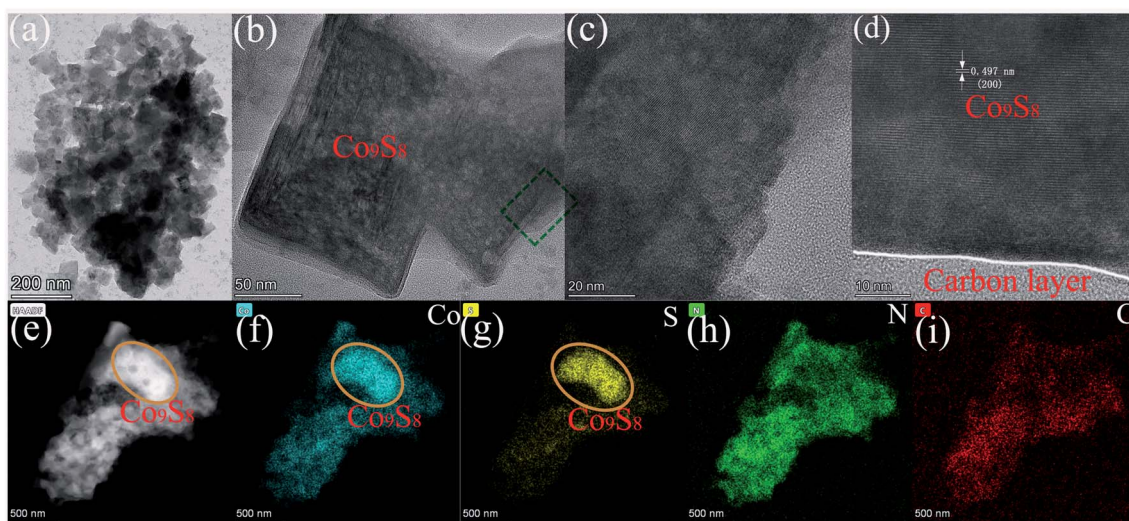

Fig. 4 (a–d) The TEM images of the Co_9S_8@NS-C-900 composite under different magnifications. (e–i) The HAADF and EDS mapping images of selected regions: Co, S, N, and C.

HAADF (high-angle annular dark-field) image and EDS mappings displayed in Fig. 4e–i, it can be seen that Co, S, N and C elements are uniformly distributed in the N,S-dual-doped carbon nanoflakes. From both HAADF image and EDS mappings of Co and S elements (Fig. 4e–g), Co_9S_8 nanoparticles are also clearly visible by highlights. Based on SEM and TEM results, it can be concluded that Co_9S_8 nanoparticles are successfully embedded in N,S-dual-doped carbon nanoflakes.

3.3. HER electrocatalytic activity of the Co_9S_8@NS-C-900 composite

As the porous feature of the Co_9S_8@NS-C-900 composite is suitable for electrolyte transportation, HER electrocatalytic activities of the as-prepared sample were tested in the KOH (1 M) solution. HER polarization curves of various catalysts (including benchmark 20% Pt/C, **Co-MOF**-1000, **Co-MOF**-900 and **Co-MOF**-800) were obtained from LSV (5 mV s^{-1}). From

Fig. 5a, it can be seen that Co_9S_8@NS-C-900 shows the smallest onset potential (E_{onset}) of ca. −4.8 mV at 1 mA cm^{-2} current density, smaller than that of **Co-MOF**-1000 (E_{onset} = −54 mV) and **Co-MOF**-800 (E_{onset} = −108 mV), and close to Pt/C (E_{onset} = 0 mV). To deliver a 10.0 mA cm^{-2} current density, the operating overpotential of Co_9S_8@NS-C-900 is −86.4 mV. This is lower than that for **Co-MOF**-1000 (−176 mV), **Co-MOF**-800 (−292 mV), several reported noble-metal-free HER catalysts,[5–12,15,17] and also close to most Pt/C catalysts (−41.6 mV). To evaluate the HER kinetics of these catalysts for comparing with the benchmark Pt/C, Tafel slopes were extracted from the LSV curves. From Fig. 5b, it can be seen that the Tafel slopes obey the following sequence: Pt/C (44.8 mV dec^{-1}) < Co_9S_8@NS-C-900 (81.1 mV dec^{-1}) < **Co-MOF**-1000 (116.3 mV dec^{-1}) < **Co-MOF**-800 (182.2 mV dec^{-1}), which is consistent with the results from Fig. 5a. The Co_9S_8@NS-C-900 composite has the smallest Tafel slope among the three **Co-MOF**-derived catalysts and is close to that of Pt/C, showing efficient HER kinetics. The Tafel value of Co_9S_8@NS-C-900 also confirms that the HER mechanism abides by a Volmer–Heyrovský pathway, which means that the HER rate-determining progress depends on H_2 desorption by H_{ads} reacting with H_3O^+. The HER inherent activities of these catalysts were evaluated by the exchange current densities (J_0) extracted from the Tafel slopes by applying the extrapolation method. The J_0 value of 0.40 mA cm^{-2} for Co_9S_8@NS-C-900

outperforms the values of 0.30 mA cm^{-2} for **Co-MOF**-1000, and 0.26 mA cm^{-2} for **Co-MOF**-800, and only a little lower than that of Pt/C with the value of 0.54 mA cm^{-2}, but the value is higher than that for most of the reported noble-metal-free HER catalysts.[5–12,15,17] Therefore, the Co_9S_8@NS-C-900 catalyst has a small overpotential, a small Tafel slope and a large J_0 value, which was integrated to evaluate its efficient electrocatalytic activity towards HER. The comparison of the HER activity for some cobalt-based materials reported in literature is listed in Table S2 (ESI†). From the table, the HER catalytic performance of Co_9S_8@NS-C-900 is better than that of most of similar Co_9S_8, and its composite catalysts under alkaline conditions. It can also match most of the other cobalt-based HER catalysts, but is lower than that for some high-performance materials.

Long-term durability is a key factor to evaluate the catalyst performance. Therefore, the cyclability of the Co_9S_8@NS-C-900 catalyst was tested. In Fig. 5c, the Co_9S_8@NS-C-900 catalyst displays excellent cycling stability, and there is almost no loss in the HER activity after 1000 potential cycles. Furthermore, the long-term durability of the Co_9S_8@NS-C-900 catalyst was also evaluated by chronoamperometric measurements. As displayed in the i–t (current–time) plot (Fig. 5c, inset), the Co_9S_8@NS-C-900 catalyst retains 99.5% of the initial current after 48 h, also indicating that it exhibits excellent cycling stability in the KOH solution. Furthermore, the EIS of three **Co-MOF**-derived

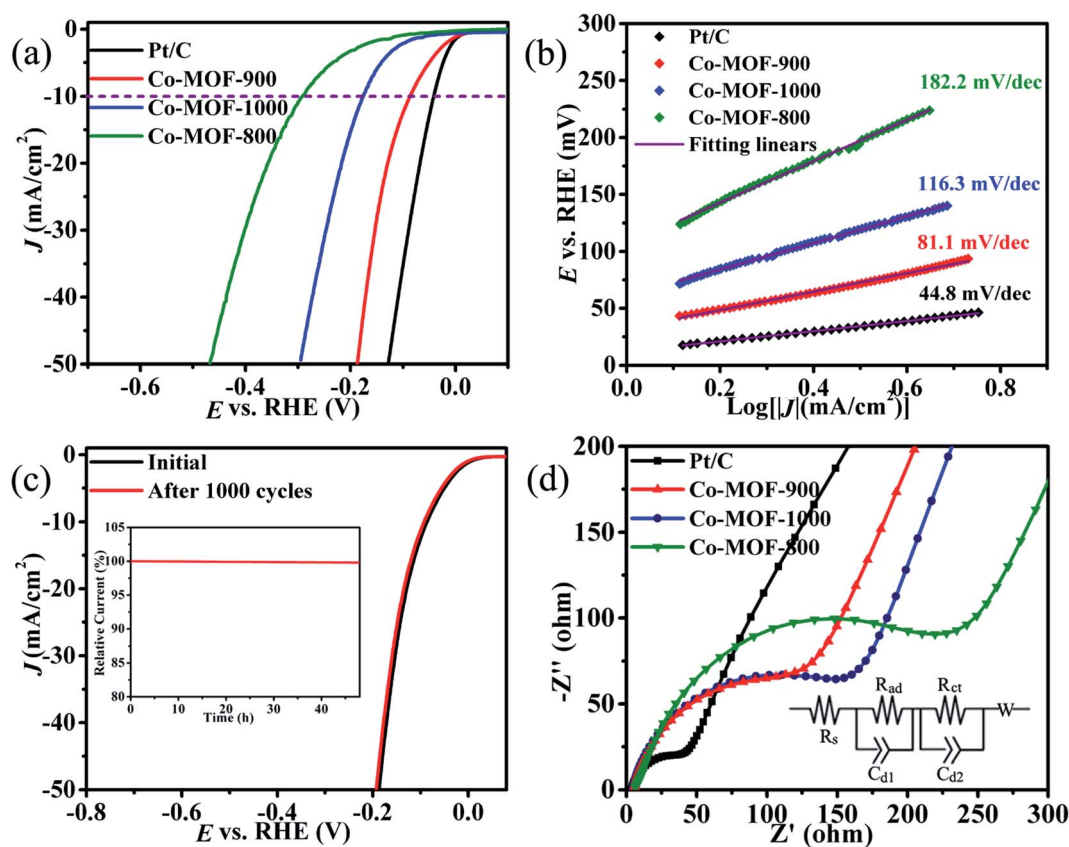**Fig. 5** (a) LSV curves of three **Co-MOF**-derived materials and Pt/C (1 M KOH). (b) Tafel slopes were obtained from the LSV curves of three **Co-MOF**-derived catalysts and Pt/C. (c) LSV plots of the Co_9S_8@NS-C-900 catalyst before and after 1000 cycles (inset: the i–t (current–time) chronoamperometry plot). (d) EIS plots of three **Co-MOF** derived catalysts and 20% Pt/C (inset: simulated equivalent circuit).

catalysts and Pt/C were also tested to estimate their catalytic kinetics. From Fig. 5d, Nyquist curves are presented for these electrocatalysts. We know that Nyquist radius could respond to R_{ct} (charge transfer resistance) and can effectively estimate the electrocatalytic activities. From Fig. 5d, 20% Pt/C has the smallest radius among all catalysts, which is consistent with its best electrocatalytic activity as a commonly accepted benchmark of HER. In three **Co-MOF**-derived catalysts, the Co_9S_8@NS-C-900 catalyst has the smallest radius than that of others and a little larger than that of Pt/C, which displayed slightly worse HER performance than Pt/C and the best HER electrocatalytic performance among three **Co-MOF**-derived species. The simulated equivalent circuit (Fig. 5d inset) was also built by fitting the ESI data, and it is composed of three resistances: the solution resistance (R_s), hydrogen adsorption resistance (R_{ad}), and R_{ct}. Due to the same equipment and outer solutions, R_s and R_{ad} are supposed to be quite similar. R_{ct} of **Co-MOF**-1000, **Co-MOF**-900, and **Co-MOF**-800 are 361.2, 145.8 and 663.2 Ω, respectively. The smallest R_{ct} of the **Co-MOF**-900 electrode among them suggests its fastest reaction kinetics during the HER process. All told, the Co_9S_8@NS-C-900 composite is an efficient HER catalyst possessing excellent cycling stabilities and superior electrocatalytic activities.

4. Conclusion

In conclusion, a porous Co_9S_8@NS-C-900 composite was fabricated by the pyrolysis of crystalline **Co-MOF** involving thiourea. The N,S-dual-doped carbon shell can protect Co_9S_8 nanoparticles from corrosion and aggregation by encapsulating them, and further prompt the stability and conductivity of the whole electrocatalyst. Therefore, benefiting from the synergistic interaction of Co_9S_8 nanoparticles and N,S-dual-doped carbon substrate, the Co_9S_8@NS-C-900 composite exhibits efficient electrocatalytic activities and long-term durability towards HER in alkaline electrolytes. In particular, the electrocatalyst requires a small overpotential of -86.4 mV at a 10.0 mA cm^{-2} current density, a small Tafel slope of 81.1 mV dec^{-1}, and a large exchange current density (J_0) of 0.40 mA cm^{-2}, representing a promising noble-free-metal electrocatalyst that approaches the performance of the state-of-the-art Pt/C electrocatalyst.

Author contributions

Yun-Wu Li: conceptualization, investigation, funding acquisition, writing-original draft. Qian Wu: data curation, project administration. Rui-Cong Ma: project administration, validation. Xiao-Qi Sun: investigation, data curation. Dan-Dan Li: formal analysis, resources. Hong-Mei Du: methodology, writing-review & editing. Hui-Yan Ma: supervision, conceptualization, visualization, writing-review & editing. Da-Cheng Li: writing-review & editing. Su-Na Wang: supervision, validation, funding acquisition, writing-review & editing. Jian-Min Dou: conceptualization, writing-review & editing. All the authors gave their final approval for publication.

Conflicts of interest

The authors declare that they have no known competing financial interests or personal relationships that could have appeared to influence the work reported in this paper.

Acknowledgements

References

1 (a) Z. W. Seh, J. Kibsgaard, C. F. Dickens, I. Chorkendorff, J. K. Norskov and T. F. Jaramillo, Combining theory and experiment in electrocatalysis: Insights into materials design, *Science*, 2017, **355**, eaad4998; (b) Y. Zheng, Y. Jiao, A. Vasileff and S. Z. Qiao, The Hydrogen Evolution Reaction in Alkaline Solution: From Theory, Single Crystal Models, to Practical Electrocatalysts, *Angew. Chem., Int. Ed.*, 2018, **57**, 7568–7579; (c) W. J. Jiang, T. Tang, Y. Zhang and J. S. Hu, Synergistic Modulation of Non-Precious-Metal Electrocatalysts for Advanced Water Splitting, *Acc. Chem. Res.*, 2020, **53**, 1111–1123; (d) C. L. Hu, L. Zhang and J. L. Gong, Recent progress made in the mechanism comprehension and design of electrocatalysts for alkaline water splitting, *Energy Environ. Sci.*, 2019, **12**, 2620–2645; (e) C. Wei, R. R. Rao, J. Y. Peng, B. T. Huang, I. E. L. Stephens, M. Risch, Z. C. J. Xu and S. H. Yang, Recommended Practices and Benchmark Activity for Hydrogen and Oxygen Electrocatalysis in Water Splitting and Fuel Cells, *Adv. Mater.*, 2019, **31**, 1806296; (f) J. Zhang, Q. Y. Zhang and X. L. Feng, Support and Interface Effects in Water-Splitting Electrocatalysts, *Adv. Mater.*, 2019, **31**, 1808167.

2 (a) J. Zhu, L. S. Hu, P. X. Zhao, L. Y. Suk Lee and K. Y. Wong, Recent Advances in Electrocatalytic Hydrogen Evolution Using Nanoparticles, *Chem. Rev.*, 2020, **120**, 851–918; (b) C. G. Morales-Guio, L. A. Stern and X. L. Hu, Nanostructured hydrotreating catalysts for electrochemical hydrogen evolution, *Chem. Soc. Rev.*, 2014, **43**, 6555–6569; (c) J. A. Trindell, Z. Y. Duan, G. Henkelman and R. M. Crooks, Well-Defined Nanoparticle Electrocatalysts for the Refinement of Theory, *Chem. Rev.*, 2020, **120**, 814–850; (d) T. Y. Wang, H. Xie, M. J. Chen, A. D'Aloia, J. Choc, G. Wu and Q. Li, Precious metal-free approach to hydrogen electrocatalysis for energy conversion: From mechanism understanding to catalyst design, *Nano Energy*, 2017, **42**, 69–89; (e) X. C. Du, J. W. Huang, J. J. Zhang, Y. C. Yan, C. Y. Wu, Y. Hu, C. Y. Yan, T. Y. Lei, W. Chen, C. Fan and J. Xiong, Modulating Electronic Structures of Inorganic Nanomaterials for Efficient Electrocatalytic Water Splitting, *Angew. Chem., Int. Ed.*, 2019, **58**, 4484–4502; (f) B. Ginovska-Pangovska, A. Dutta, M. L. Reback, J. C. Linehan and

W. J. Shaw, Beyond the active site: the impact of the outer coordination sphere on electrocatalysts for hydrogen production and oxidation, *Acc. Chem. Res.*, 2014, **47**, 2621–2630.

3 (*a*) Z. X. Fan and H. Zhang, Template Synthesis of Noble Metal Nanocrystals with Unusual Crystal Structures and Their Catalytic Applications, *Acc. Chem. Res.*, 2016, **49**, 2841–2850; (*b*) L. Zhang, K. Doyle-Davis and X. L. Sun, Pt-Based Electrocatalysts with High Atom Utilization Efficiency: From Nanostructures to Single Atoms, *Energy Environ. Sci.*, 2019, **12**, 492–517; (*c*) Y. J. Li, Y. J. Sun, Y. N. Qin, W. Y. Zhang, L. Wang, M. C. Luo, H. Yang and S. J. Guo, Recent Advances on Water Splitting Electrocatalysis Mediated by Noble-Metal-Based Nanostructured Materials, *Adv. Energy Mater.*, 2020, **10**, 1903120; (*d*) Y. X. Du, H. T. Sheng, D. Astruc and M. Z. Zhu, Atomically Precise Noble Metal Nanoclusters as Efficient Catalysts: A Bridge between Structure and Properties, *Chem. Rev.*, 2020, **120**, 526–622.

4 (*a*) J. Kim, H. Kim, W. J. Lee, B. Ruqia, H. Baik, H. S. Oh, S. M. Paek, H. K. Lim, C. H. Choi and S. I. Choi, Theoretical and Experimental Understanding of Hydrogen Evolution Reaction Kinetics in Alkaline Electrolytes with Pt-Based Core-Shell Nanocrystals, *J. Am. Chem. Soc.*, 2019, **141**, 18256–18263; (*b*) Q. Yang, G. W. Li, K. Manna, F. R. Fan, C. Felser and Y. Sun, Topological Engineering of Pt-Group-Metal-Based Chiral Crystals toward High-Efficiency Hydrogen Evolution Catalysts, *Adv. Mater.*, 2020, **32**, 1908518; (*c*) J. Park, S. Lee, H. E. Kim, A. Cho, S. Kim, Y. Ye, J. W. Han, H. Lee, J. H. Jang and J. Lee, Investigation of the Support Effect in Atomically Dispersed Pt on WO$_{3-x}$ for Utilization of Pt in the Hydrogen Evolution Reaction, *Angew. Chem., Int. Ed.*, 2019, **58**, 16038–16042; (*d*) A. Alinezhad, L. Gloag, T. M. Benedetti, S. Cheong, R. F. Webster, M. Roelsgaard, B. B. Iversen, W. Schuhmann, J. J. Gooding and R. D. Tilley, Direct Growth of Highly Strained Pt Islands on Branched Ni Nanoparticles for Improved Hydrogen Evolution Reaction Activity, *J. Am. Chem. Soc.*, 2019, **141**, 16202–16207; (*e*) J. P. Ji, Y. P. Zhang, L. B. Tang, C. Y. Liu, X. H. Gao, M. H. Sun, J. H. Zheng, M. Ling, C. D. Liang and Z. Lin, Platinum single-atom and cluster anchored on functionalized MWCNTs with ultrahigh mass efficiency for electrocatalytic hydrogen evolution, *Nano Energy*, 2019, **63**, 103849.

5 (*a*) D. Zhao, K. Sun, W. C. Cheong, L. R. Zheng, C. Zhang, S. J. Liu, X. Cao, K. L. Wu, Y. Pan, Z. W. Zhuang, B. T. Hu, D. S. Wang, Q. Peng, C. Chen and Y. D. Li, Synergistically Interactive Pyridinic–N–MoP Sites: Identified Active Centers for Enhanced Hydrogen Evolution in Alkaline Solution, *Angew. Chem., Int. Ed.*, 2020, **59**, 8982–8990; (*b*) C. Huang, X. W. Miao, C. R. Pi, B. Gao, X. M. Zhang, P. Qin, K. F. Huo, X. Peng and P. K. Chu, Mo$_2$C/VC heterojunction embedded in graphitic carbon network: An advanced electrocatalyst for hydrogen evolution, *Nano Energy*, 2019, **60**, 520–526; (*c*) F. Li, G. F. Han, H. J. Noh, Y. L. Lu, J. Xu, Y. F. Bu, Z. P. Fu and J. B. Baek, Construction of Porous Mo$_3$P/Mo Nanobelts as Catalysts for Efficient Water Splitting, *Angew. Chem., Int. Ed.*, 2018, **57**, 14139–14143; (*d*) Z. X. Sun, M. F. Yang, Y. W. Wang and Y. H. Hu, Novel Binder-Free Three-Dimensional MoS$_2$-Based Electrode for Efficient and Stable Electrocatalytic Hydrogen Evolution, *ACS Appl. Energy Mater.*, 2019, **2**, 1102–1110; (*e*) J. S. Li, Y. Wang, C. H. Liu, S. L. Li, Y. G. Wang, L. Z. Dong, Z. H. Dai, Y. F. Li and Y. Q. Lan, Coupled molybdenum carbide and reduced graphene oxide electrocatalysts for efficient hydrogen evolution, *Nat. Commun.*, 2016, **7**, 11204; (*f*) D. Z. Wang, D. Z. Zhang, C. Y. Tang, P. Zhou, Z. Z. Wu and B. Z. Fang, Hydrogen evolution catalyzed by cobalt-promoted molybdenum phosphide nanoparticles, *Catal. Sci. Technol.*, 2016, **6**, 1952–1956; (*g*) Z. Z. Wu, C. Y. Tang, P. Zhou, Z. H. Liu, Y. S. Xu, D. Z. Wang and B. Z. Fang, Enhanced hydrogen evolution catalysis from osmotically swollen ammoniated MoS$_2$, *J. Mater. Chem. A*, 2015, **3**, 13050–13056.

6 (*a*) M. A. Lukowski, A. S. Daniel, C. R. English, F. Meng, A. Forticaux, R. J. Hamers and S. Jin, Highly active hydrogen evolution catalysis from metallic WS$_2$ nanosheets, *Energy Environ. Sci.*, 2014, **7**, 2608–2613; (*b*) L. Cheng, W. J. Huang, Q. F. Gong, C. H. Liu, Z. Liu, Y. G. Li and H. J. Dai, Ultrathin WS$_2$ Nanoflakes as a High-Performance Electrocatalyst for the Hydrogen Evolution Reaction, *Angew. Chem., Int. Ed.*, 2014, **53**, 7860–7863; (*c*) H. J. Yan, C. G. Tian, L. Wang, A. P. Wu, M. C. Meng, L. Zhao and H. G. Fu, Phosphorus-Modified Tungsten Nitride/Reduced Graphene Oxide as a High-Performance, Non-Noble-Metal Electrocatalyst for the Hydrogen Evolution Reaction, *Angew. Chem., Int. Ed.*, 2015, **54**, 6325–6329; (*d*) Y. Y. Ma, Z. L. Lang, L. K. Yan, Y. H. Wang, H. Q. Tan, K. Feng, Y. J. Xia, J. Zhong, Y. Liu, Z. H. Kang and Y. G. Li, High efficient hydrogen evolution triggered by a multi-interfacial Ni/WC hybrid electrocatalyst, *Energy Environ. Sci.*, 2018, **11**, 2114–2123; (*e*) Z. G. Chen, W. B. Gong, S. Cong, Z. Wang, G. Song, T. Pan, X. Q. Tang, J. Chen, W. B. Lu and Z. G. Zhao, Eutectoid-structured WC/W$_2$C heterostructures: A new platform for long-term alkaline hydrogen evolution reaction at low overpotentials, *Nano Energy*, 2020, **68**, 104335.

7 (*a*) S. Anantharaj and V. Aravindan, Developments and Perspectives in 3d Transition-Metal-Based Electrocatalysts for Neutral and Near-Neutral Water Electrolysis, *Adv. Energy Mater.*, 2019, **9**, 1902666; (*b*) V. S. Thoi, Y. J. Sun, J. R. Long and C. J. Chang, Complexes of earth-abundant metals for catalytic electrochemical hydrogen generation under aqueous conditions, *Chem. Soc. Rev.*, 2013, **42**, 2388–2400; (*c*) Y. M. Shi and B. Zhang, Recent advances in transition metal phosphide nanomaterials: synthesis and applications in hydrogen evolution reaction, *Chem. Soc. Rev.*, 2016, **45**, 1529–1541; (*d*) Y. N. Guo, T. Park, J. W. Yi, J. Henzie, J. Kim, Z. L. Wang, B. Jiang, Y. Bando, Y. Sugahara, J. Tang and Y. Yamauchi, Nanoarchitectonics for Transition-Metal-Sulfide-Based Electrocatalysts for Water Splitting, *Adv. Mater.*, 2019, **31**, 1807134; (*e*) J. H. Wang, W. Cui, Q. Liu, Z. C. Xing, A. M. Asiri and

X. P. Sun, Recent Progress in Cobalt-Based Heterogeneous Catalysts for Electrochemical Water Splitting, *Adv. Mater.*, 2016, **28**, 215–230.

8 (a) Y. R. Zheng, P. Wu, M. R. Gao, X. L. Zhang, F. Y. Gao, H. X. Ju, R. Wu, Q. Gao, R. You, W. X. Huang, S. J. Liu, S. W. Hu, J. F. Zhu, Z. Y. Li and S. H. Yu, Doping induced structural phase transition in cobalt diselenide enables enhanced hydrogen evolution catalysis, *Nat. Commun.*, 2018, **9**, 2533; (b) X. Zou, X. Huang, A. Goswami, R. Silva, B. R. Sathe, E. Mikmekova and T. Asefa, Cobalt-Embedded Nitrogen-Rich Carbon Nanotubes Efficiently Catalyze Hydrogen Evolution Reaction at All pH Values, *Angew. Chem., Int. Ed.*, 2014, **53**, 4372–4376; (c) J. X. Feng, S. Y. Tong, Y. X. Tong and G. R. Li, Pt-like Hydrogen Evolution Electrocatalysis on PANI/CoP Hybrid Nanowires by Weakening the Shackles of Hydrogen Ions on the Surfaces of Catalysts, *J. Am. Chem. Soc.*, 2018, **140**, 5118–5126; (d) C. Tang, R. Zhang, W. B. Lu, L. B. He, X. E. Jiang, A. M. Asiri and X. P. Sun, Fe-Doped CoP Nanoarray: A Monolithic Multifunctional Catalyst for Highly Efficient Hydrogen Generation, *Adv. Mater.*, 2017, **29**, 1602441; (e) T. Liu, P. Li, N. Yao, G. Z. Cheng, S. L. Chen, W. Luo and Y. D. Yin, CoP-Doped MOF-Based Electrocatalys for pH-Universal Hydrogen Evolution Reaction, *Angew. Chem., Int. Ed.*, 2019, **58**, 4679–4684.

9 (a) K. Srinivas, Y. J. Lu, Y. F. Chen, W. L. Zhang and D. X. Yang, FeNi$_3$-Fe$_3$O$_4$ Heterogeneous Nanoparticles Anchored on 2D MOF Nanosheets/1D CNT Matrix as Highly Efficient Bifunctional Electrocatalysts for Water Splitting, *ACS Sustainable Chem. Eng.*, 2020, **8**, 3820–3831; (b) D. Y. Chung, S. W. Jun, G. Yoon, H. Kim, J. M. Yoo, K. S. Lee, T. Kim, H. Shin, A. K. Sinha, S. G. Kwon, K. Kang, T. Hyeon and Y. E. Sung, Large-Scale Synthesis of Carbon-Shell-Coated FeP Nanoparticles for Robust Hydrogen Evolution Reaction Electrocatalyst, *J. Am. Chem. Soc.*, 2017, **139**, 6669–6674; (c) X. H. Fan, F. T. Kong, A. G. Kong, A. L. Chen, Z. Q. Zhou and Y. K. Shan, Covalent Porphyrin Framework-Derived Fe$_2$P@Fe$_4$N-Coupled Nanoparticles Embedded in N-Doped Carbons as Efficient Trifunctional Electrocatalysts, *ACS Appl. Mater. Interfaces*, 2017, **9**, 32840–32850; (d) J. Jin, J. Yin, H. B. Liu, M. Lu, J. Y. Li, M. Tian and P. X. Xi, Transition Metal (Fe, Co and Ni)-Carbide-Nitride (M-C-N) Nanocatalysts: Structure and Electrocatalytic Applications, *ChemCatChem*, 2019, **11**, 2780–2792; (e) J. Y. Yu, G. X. Li, H. Liu, L. L. Zeng, L. L. Zhao, J. Jia, M. Y. Zhang, W. J. Zhou, H. Liu and Y. Y. Hu, Electrochemical Flocculation Integrated Hydrogen Evolution Reaction of Fe@N-Doped Carbon Nanotubes on Iron Foam for Ultralow Voltage Electrolysis in Neutral Media, *Adv. Sci.*, 2019, **6**, 1901458.

10 (a) R. Subbaraman, D. Tripkovic, D. Strmcnik, K. C. Chang, M. Uchimura, A. P. Paulikas, V. Stamenkovic and N. M. Markovic, Enhancing Hydrogen Evolution Activity in Water Splitting by Tailoring Li$^+$-Ni(OH)$_2$-Pt Interfaces, *Science*, 2011, **334**, 1256–1260; (b) D. D. Zhang, J. Y. Shi, Y. Qi, X. M. Wang, H. Wang, M. R. Li, S. Z. Liu and C. Li, Quasi-Amorphous Metallic Nickel Nanopowder as an Efficient and Durable Electrocatalyst for Alkaline Hydrogen Evolution, *Adv. Sci.*, 2018, **5**, 1801216; (c) C. J. Lei, Y. Wang, Y. Hou, P. Liu, J. Yang, T. Zhang, X. D. Zhuang, M. W. Chen, B. Yang, L. C. Lei, C. Yuan, M. Qiu and X. L. Feng, Efficient Alkaline Hydrogen Evolution on Atomically Dispersed Ni–N$_x$ Species Anchored Porous Carbon with Embedded Ni Nanoparticles by Accelerating Water Dissociation Kinetics, *Energy Environ. Sci.*, 2019, **12**, 149–156; (d) Z. Fang, L. Peng, Y. Qian, X. Zhang, Y. Xie, J. J. Cha and G. Yu, Dual Tuning of Ni-Co-A (A = P, Se, O) Nanosheets by Anion Substitution and Holey Engineering for Efficient Hydrogen Evolution, *J. Am. Chem. Soc.*, 2018, **140**, 5241–5247; (e) Y. B. Li, X. Tan, S. Chen, X. Bo, H. J. Ren, S. C. Smith and C. Zhao, Processable Surface Modification of Nickel-Heteroatom (N, S) Bridge Sites for Promoted Alkaline Hydrogen Evolution, *Angew. Chem., Int. Ed.*, 2019, **58**, 461–466.

11 (a) R. Paul, L. Zhu, H. Chen, J. Qu and L. M. Dai, Recent Advances in Carbon-Based Metal-Free Electrocatalysts, *Adv. Mater.*, 2019, **31**, 1806403; (b) B. R. Sathe, X. X. Zou and T. Asefa, Metal-free B-doped graphene with efficient electrocatalytic activity for hydrogen evolution reaction, *Catal. Sci. Technol.*, 2014, **4**, 2023–2030; (c) K. G. Qu, Y. Zheng, X. X. Zhang, K. Davey, S. Dai and S. Z. Qiao, Promotion of Electrocatalytic Hydrogen Evolution Reaction on Nitrogen-Doped Carbon Nanosheets with Secondary Heteroatoms, *ACS Nano*, 2017, **11**, 7293–7300; (d) L. Z. Zhang, Y. Jia, X. C. Yan and X. D. Yao, Activity Origins in Nanocarbons for the Electrocatalytic Hydrogen Evolution Reaction, *Small*, 2018, **14**, 1800235; (e) F. Xiao, Z. M. Chen, H. Wu, Y. Wang, E. P. Cao, X. D. Lu, Y. Q. Wu and Z. Y. Ren, Phytic Acid-Guided Ultra-Thin N,P Co-Doped Carbon Coated Carbon Nanotubes for Efficient All-pH Electrocatalytic Hydrogen Evolution, *Nanoscale*, 2019, **11**, 23027–23034.

12 (a) H. L. Fei, J. C. Dong, D. L. Chen, T. D. Hu, X. D. Duan, I. Shakir, Y. Huang and X. F. Duan, Single atom electrocatalysts supported on graphene or graphene-like carbons, *Chem. Soc. Rev.*, 2019, **48**, 5207–5241; (b) Z. S. Shi, W. Q. Yang, Y. T. Gu, T. Liao and Z. Q. Sun, Metal-Nitrogen-Doped Carbon Materials as Highly Efficient Catalysts: Progress and Rational Design, *Adv. Sci.*, 2020, **7**, 2001069; (c) X. J. Zhu, J. L. Dai, L. G. Li, D. K. Zhao, Z. X. Wu, Z. H. Tang, L. J. Ma and S. W. Chen, Hierarchical carbon microflowers supported defect-rich Co3S4 nanoparticles: An efficient electrocatalyst for water splitting, *Carbon*, 2020, **160**, 133–144; (d) X. P. Gao, Y. A. Zhou, S. Q. Liu, Z. W. Cheng, Y. J. Tan and Z. M. Shen, Single Cobalt Atom Anchored on N-Doped Graphyne for Boosting the Overall Water Splitting, *Appl. Surf. Sci.*, 2020, **502**, 144155; (e) S. V. Mohite, R. M. Xing, B. Y. Li, S. S. Latthe, Y. Zhao, X. Y. Li, L. Q. Mao and S. H. Liu, Spatial Compartmentalization of Cobalt Phosphide in P-Doped Dual Carbon Shells for Efficient Alkaline Overall Water Splitting, *Inorg. Chem.*, 2020, **59**, 1996–2004; (f) S. Yu, S. L. Song, R. Li and B. Z. Fang, The lightest solid meets the lightest gas: an overview of carbon

aerogels and their composites for hydrogen related applications, *Nanoscale*, 2020, **12**, 19536–19556.

13 (*a*) G. F. Liao, Y. Gong, L. Zhang, H. Y. Gao, G. J. Yang and B. Z. Fang, Semiconductor polymeric graphitic carbon nitride photocatalysts: the "holy grail" for the photocatalytic hydrogen evolution reaction under visible light, *Energy Environ. Sci.*, 2019, **12**, 2080–2147; (*b*) G. F. Liao, J. S. Fang, Q. Li, S. H. Li, Z. S. Xu and B. Z. Fang, Ag-Based nanocomposites: synthesis and applications in catalysis, *Nanoscale*, 2019, **11**, 7062–7096; (*c*) G. Q. Suo, J. Q. Zhang, D. Li, Q. Y. Yu, W. A. Wang, M. He, L. Feng, X. J. Hou, Y. L. Yang, X. H. Ye and L. Zhang, N-doped carbon/ultrathin 2D metallic cobalt selenide core/sheath flexible framework bridged by chemical bonds for high-performance potassium storage, *Chem. Eng. J.*, 2020, **388**, 124396; (*d*) D. Li, J. Q. Zhang, S. M. Ahmed, G. Q. Suo, W. A. Wang, L. Feng, X. J. Hou, Y. L. Yang, X. H. Ye and L. Zhang, Amorphous carbon coated SnO$_2$ nanohseets on hard carbon hollow spheres to boost potassium storage with high surface capacitive contributions, *J. Colloid Interface Sci.*, 2020, **574**, 174–181; (*e*) G. Q. Suo, J. Q. Zhang, D. Li, Q. Y. Yu, M. He, L. Feng, X. J. Hou, Y. L. Yang, X. H. Ye, L. Zhang and W. A. Wang, *J. Colloid Interface Sci.*, 2020, **566**, 427–433; (*f*) X. F. Wang, H. X. Liu, Q. Wang, J. H. Huo, W. Y. Ge, X. B. Duan and S. Q. Guo, *Appl. Surf. Sci.*, 2021, **540**, 148351.

14 (*a*) X. M. Guo, W. Zhang, D. Zhang, S. L. Qian, X. Z. Tong, D. C. Zhou, J. H. Zhang and A. H. Yuan, Co$_9$S$_8$/CoS/C submicron-spheres derived from bacteria for electrocatalytic oxygen reduction reaction, *ChemElectroChem*, 2019, **6**, 4571–4575; (*b*) X. F. Liu, C. C. Hao, L. H. He, C. Yang, Y. B. Chen, C. B. Jiang and R. H. Yu, Yolk-shell structured Co-C/Void/Co$_9$S$_8$ composites witha tunable cavity for ultrabroad band and efficient low-frequency microwave absorption, *Nano Res.*, 2018, **11**, 4169–4182; (*c*) P. Y. Zeng, J. W. Li, M. Ye, K. F. Zhuo and Z. Fang, In Situ Formation of Co$_9$S$_8$/N-C Hollow Nanospheres by Pyrolysis and Sulfurization of ZIF-67 for High-Performance Lithium-Ion Batteries, *Chem.–Eur. J.*, 2017, **23**, 9517–9524; (*d*) Y. Y. Zhao, Q. Fu, D. S. Wang, Q. Pang, Y. Gao, A. Missiul, R. Nemausat, A. Sarapulova, H. Ehrenberg, Y. J. Wei and G. Chen, Co9S8@carbon yolk-shell nanocages as a high performance direct conversion anode material for sodium ion batteries, *Energy Storage Materials*, 2019, **18**, 51–58; (*e*) H. X. Zhong, K. Li, Q. Zhang, J. Wang, F. L. Meng, Z. J. Wu, J. M. Yan and X. B. Zhang, In situ anchoring of Co$_9$S$_8$ nanoparticles on N and S co-doped porous carbon tube as bifunctional oxygen electrocatalysts, *NPG Asia Mater.*, 2016, **8**, e308.

15 (*a*) J. Du, R. Wang, Y. R. Lv, Y. L. Wei and S. Q. Zang, One-step MOF-derived Co/Co$_9$S$_8$ nanoparticles embedded in nitrogen, sulfur and oxygen ternary-doped porous carbon: an efficient electrocatalyst for overall water splitting, *Chem. Commun.*, 2019, **55**, 3203–3206; (*b*) N. Huang, S. F. Yan, M. Y. Zhang, Y. Y. Ding, L. Yang, P. P. Sun and X. H. Sun, A MoS$_2$-Co$_9$S$_8$-NC heterostructure as an efficient bifunctional electrocatalyst towards hydrogen and oxygen evolution

reaction, *Electrochim. Acta*, 2019, **327**, 134942; (*c*) H. Yu, X. Y. Sun, D. H. Tang, Y. Huang, W. T. Zhang, S. J. Miao, Z. A. Qiao, J. J. Wang and Z. Zhao, Molten salt strategy to synthesize alkali metal doped Co$_9$S$_8$ nanoparticles embedded, N, S co-doped mesoporous carbon as hydrogen evolution electrocatalyst, *Int. J. Hydrogen Energy*, 2020, **45**, 6006–6014; (*d*) L. G. Wang, X. X. Duan, X. J. Liu, J. Gu, R. Si, Y. Qiu, Y. M. Qiu, D. E. Shi, F. H. Chen, X. M. Sun, J. H. Lin and J. L. Sun, Atomically Dispersed Mo Supported on Metallic Co$_9$S$_8$ Nanoflakes as an Advanced Noble-Metal-Free Bifunctional Water Splitting Catalyst Working in Universal pH Conditions, *Adv. Energy Mater.*, 2019, **9**, 1903137; (*e*) J. G. Yan, L. G. Chen and X. Liang, Co$_9$S$_8$ Nanowires@NiCo LDH Nanosheets Arrays on Nickel Foams towards Efficient Overall Water Splitting, *Sci. Bull.*, 2019, **64**, 158–165.

16 (*a*) B. J. Zhu, R. Q. Zou and Q. Xu, Metal−Organic Framework Based Catalysts for Hydrogen Evolution, *Adv. Energy Mater.*, 2018, **8**, 1801193; (*b*) P. Q. Liao, J. Q. Shen and J. P. Zhang, Metal−organic frameworks for electrocatalysis, *Coord. Chem. Rev.*, 2018, **373**, 22–48; (*c*) L. J. Kong, M. Zhong, W. Shuang, Y. H. Xu and X. H. Bu, Electrochemically active sites inside crystalline porous materials for energy storage and conversion, *Chem. Soc. Rev.*, 2020, **49**, 2378–2407; (*d*) X. D. Wen and J. Q. Guan, Recent progress on MOF-derived electrocatalystsfor hydrogen evolution reaction, *Applied Materials Today*, 2019, **16**, 146–168; (*e*) H. Kobayashi, Y. Mitsuka and H. Kitagawa, Metal Nanoparticles Covered with a Metal−Organic Framework: From One-Pot Synthetic Methods to Synergistic Energy Storage and Conversion Functions, *Inorg. Chem.*, 2016, **55**, 7301–7310; (*f*) D. Liu, X. M. Zhang, Y. J. Wang, S. Y. Song, L. F. Cui, H. B. Fan, X. C. Qiao and B. Z. Fang, A new perspective of lanthanide metal−organic frameworks: tailoring Dy-BTC nanospheres for rechargeable Li−O$_2$ batteries, *Nanoscale*, 2020, **12**, 9524–9532; (*g*) Y. W. Li, W. J. Zhang, J. Li, H. Y. Ma, H. M. Du, D. C. Li, S. N. Wang, J. S. Zhao, J. M. Dou and L. Q. Xu, Fe-MOF-Derived Efficient ORR/OER Bifunctional Electrocatalyst for Rechargeable Zinc−Air Batteries, *ACS Appl. Mater. Interfaces*, 2020, **12**, 44710–44719.

17 (*a*) L. T. Yan, L. Cao, P. C. Dai, X. Gu, D. D. Liu, L. J. Li, Y. Wang and X. B. Zhao, Metal−Organic Frameworks Derived Nanotube of Nickel–Cobalt Bimetal Phosphides as Highly Efficient Electrocatalysts for Overall Water Splitting, *Adv. Funct. Mater.*, 2017, **27**, 1703455; (*b*) B. C. Weng, C. R. Grice, W. W. Meng, L. Guan, F. H. Xu, Y. Yu, C. L. Wang, D. W. Zhao and Y. F. Yan, Metal−Organic Framework-Derived CoWP@C Composite Nanowire Electrocatalyst for Efficient Water Splitting, *ACS Energy Lett.*, 2018, **3**, 1434–1442; (*c*) W. Q. Liu, Y. M. Zhou, J. H. Bao, J. Q. Wang, Y. W. Zhang, X. L. Sheng, Y. Xue, C. Guo and X. X. Chen, Co-CoO-ZnFe$_2$O$_4$ encapsulated in carbon nanowires derived from MOFs as electrocatalysts for hydrogen evolution, *J. Colloid Interface Sci.*, 2020, **561**, 620–628; (*d*) Y. J. Lei, L. Wei, S. L. Zhai, Y. Q. Wang, H. E. Karahan, X. C. Chen, Z. Zhou, C. J. Wang, X. Sui and

Y. Chen, Metal-free bifunctional carbon electrocatalysts derived from zeolitic imidazolate frameworks for efficient water splitting, *Mater. Chem. Front.*, 2018, **2**, 102–111; (*e*) Y. L. Li, B. M. Jia, B. Y. Chen, Q. L. Liu, M. K. Cai, Z. Q. Xue, Y. A. Fan, H. P. Wang, C. Y. Su and G. Q. Li, MOF-derived Mn doped porous CoP nanosheets as efficient and stable bifunctional electrocatalysts for water splitting, *Dalton Trans.*, 2018, **47**, 14679–14685.

18 H. Y. Ma, Y. Z. Zhang, H. Yan, W. J. Zhang, Y. W. Li, S. N. Wang, D. C. Li, J. M. Dou and J. R. Li, Two Microporous Co^{II}-MOFs with Dual Active Sites for Highly Selective Adsorption of CO$_2$/CH$_4$ and CO$_2$/N$_2$, *Dalton Trans.*, 2019, **48**, 13541–13545.

19 (*a*) A. C. Ferrari and D. M. Basko, Raman spectroscopy as a versatile tool for studying the properties of grapheme, *Nat. Nanotechnol.*, 2013, **8**, 235–246; (*b*) N. Sikdar, B. Konkena, J. Masa, W. Schuhmann and T. K. Maji, Co$_3$O$_4$@Co/NCNT Nanostructure Derived from a Dicyanamide-Based Metal–Organic Framework as an Efficient Bi-functional Electrocatalyst for Oxygen Reduction and Evolution Reactions, *Chem.–Eur. J.*, 2017, **23**, 18049–18056; (*c*) D. N. Ding, K. Shen, X. D. Chen, H. R. Chen, J. Y. Chen, T. Fan, R. F. Wu and Y. W. Li, Multi-Level Architecture Optimization of MOF-Templated Co-Based Nanoparticles Embedded in Hollow N-Doped Carbon Polyhedra for Efficient OER and ORR, *ACS Catal.*, 2018, **8**, 7879–7888; (*d*) S. M Alshehri, J. Ahmed, A. Khan, M. Naushad and T. Ahamad, Bifunctional Electrocatalysts (Co$_9$S$_8$@NSC) Derived from a Polymer-metal Complex for the Oxygen Reduction and Oxygen Evolution Reactions, *ChemElectroChem*, 2018, **5**, 355–361.

20 (*a*) Y. W. Li, J. Xu, D. C. Li, J. M. Dou, H. Yan, T. L. Hu and X. H. Bu, Two microporous MOFs constructed from different metal cluster SBUs for selective gas adsorption, *Chem. Commun.*, 2015, **51**, 14211–14214; (*b*) Y. W. Li, H. Yan, T. L. Hu, H. Y. Ma, D. C. Li, S. N. Wang, Q. X. Yao, J. M. Dou, J. Xu and X. H. Bu, Two microporous Fe-based MOFs with multiple active sites for selective gas adsorption, *Chem. Commun.*, 2017, **53**, 2394–2397; (*c*) D. S. Zhang, Y. Z. Zhang, X. L. Zhang, F. Wang, J. Zhang, H. Hu, J. Gao, H. Yan, H. L. Liu, H. Y. Ma, L. L. Geng and Y. W. Li, Nanocage-Based Porous Metal–Organic Frameworks Constructed from Icosahedrons and Tetrahedrons for Selective Gas Adsorption, *ACS Appl. Mater. Interfaces*, 2019, **11**, 20104–20109.

21 (*a*) N. Yao, P. Li, Z. R. Zhou, Y. M. Zhao, G. Z. Cheng, S. L. Chen and W. Luo, Synergistically Tuning Water and Hydrogen Binding Abilities Over Co$_4$N by Cr Doping for Exceptional Alkaline Hydrogen Evolution Electrocatalysis, *Adv. Energy Mater.*, 2019, **9**, 1902449; (*b*) Z. Y. Chen, Y. Song, J. Y. Cai, X. S. Zheng, D. D. Han, Y. S. Wu, Y. P. Zang, S. W. Niu, Y. Liu, J. F. Zhu, X. J. Liu and G. M. Wang, Tailoring the d-Band Centers Enables Co$_4$N Nanosheets To Be Highly Active for Hydrogen Evolution

Catalysis, *Angew. Chem., Int. Ed.*, 2018, **57**, 5076–5080; (*c*) Y. P. Wu, W. Zhou, J. Zhao, W. W. Dong, Y. Q. Lan, D. S. Li, C. H. Sun and X. H. Bu, Surfactant-Assisted Phase-Selective Synthesis of New Cobalt MOFs and Their Efficient Electrocatalytic Hydrogen Evolution Reaction, *Angew. Chem., Int. Ed.*, 2017, **56**, 13001–13005; (*d*) H. Li, P. Wen, D. S. Itanze, M. W. Kim, S. Adhikari, C. Lu, L. Jiang, Y. J. Qiu and S. M. Geyer, Phosphorus-Rich Colloidal Cobalt Diphosphide (CoP$_2$) Nanocrystals for Electrochemical and Photoelectrochemical Hydrogen Evolution, *Adv. Mater.*, 2019, **31**, 1900813; (*e*) H. P. Feng, L. Tang, G. M. Zeng, J. F. Yu, Y. C. Deng, Y. Y. Zhou, J. J. Wang, C. Y. Feng, T. Luo and B. B. Shao, Electron density modulation of Fe$_{1-x}$Co$_x$P nanosheet arrays by iron incorporation for highly efficient water splitting, *Nano Energy*, 2020, **67**, 104174.

22 (*a*) E. P. Cao, Z. M. Chen, H. Wu, P. Yu, Y. Wang, F. Xiao, S. Chen, S. C. Du, Y. Xie, Y. Q. Wu and Z. Y. Ren, Boron-Induced Electronic-Structure Reformation of CoP Nanoparticles Drives Enhanced pH-Universal Hydrogen Evolution, *Angew. Chem., Int. Ed.*, 2020, **59**, 4154–4160; (*b*) Y. Tong, X. W. Yu, H. Y. Wang, B. W. Yao, C. Li and G. Q. Shi, Trace Level Co-N Doped Graphite Foams as High-Performance Self-Standing Electrocatalytic Electrodes for Hydrogen and Oxygen Evolution, *ACS Catal.*, 2018, **8**, 4637–4644; (*c*) X. Q. Wang, J. R. He, B. Yu, B. C. Sun, D. X. Yang, X. J. Zhang, Q. H. Zhang, W. L. Zhang, L. Gu and Y. F. Chen, CoSe$_2$ nanoparticles embedded MOF-derived Co-N-C nanoflake arrays as efficient and stable electrocatalyst for hydrogen evolution reaction, *Appl. Catal., B*, 2019, **258**, 117996; (*d*) Y. J. Zhang, W. F. Li, L. H. Lu, W. G. Song, C. R. Wang, L. S. Zhou, J. H. Liu, Y. Chen, H. Y. Jin and Y. G. Zhang, Tuning active sites on cobalt/nitrogen doped graphene for electrocatalytic hydrogen and oxygen evolution, *Electrochim. Acta*, 2018, **265**, 497–506; (*e*) S. M. Wang, L. Zhang, Y. Qin, D. Ding, Y. F. Bu, F. Q. Chu, Y. Kong and M. L. Liu, Co,N-codoped graphene as efficient electrocatalyst for hydrogen evolution reaction: Insight into the active centre, *J. Power Sources*, 2017, **363**, 260–268; (*f*) X. Z. Ma, K. Y. Li, X. Zhang, B. Wei, H. Yang, L. N. Liu, M. Y. Zhang, X. T. Zhang and Y. J. Chen, The surface engineering of cobalt carbide spheres through N, B co-doping achieved by room-temperature in situ anchoring effects for active and durable multifunctional electrocatalysts, *J. Mater. Chem. A*, 2019, **7**, 14904–14915.

23 (*a*) J. R. He, Y. F. Chen and A. Manthiram, Vertical Co$_9$S$_8$ hollow nanowall arrays grown on Celgard separator as a multifunctional polysulfide barrier for high-performance Li-S batteries, *Energy Environ. Sci.*, 2018, **11**, 2560–2568; (*b*) W. Xiong, K. Hu, Z. Li, Y. X. Jiang, Z. G. Li, Z. Li and X. W. Wang, A wearable system based on core-shell structured peptide-Co$_9$S$_8$ supercapacitor and triboelectric nanogenerator, *Nano Energy*, 2019, **66**, 104149.